Bulletin of Engineering Geology and the Environment (2022) 81:31
https://doi.org/10.1007/s10064-021-02500-2

ORIGINAL PAPER

3D DEM analysis of analogue proppant–fractured rock system interaction

S. S. Kasyap[1] · H. He[2] · K. Senetakis[1]

Received: 18 June 2021 / Accepted: 14 November 2021

Abstract

We investigated the interaction of proppant simulant (impactor) colliding on the surface of a fractured rock by performing 3-dimensional discrete-based numerical simulations. The fractured rock represented a medium-strength clastic material, and the linear parallel bond contact model was implemented to simulate the bonding properties. The ratio of the impactor to rock particle size was equal to 30, which represents, based on the relative dimensions of the problem, typical proppants of 40/70 mesh colliding on fine-grained siltstone. A parametric study was conducted, taking into account the influence of existing fractures within the rock mass as well as their aperture and distance from the impact zone. Significant differences were observed based on the collision velocity (with a distinction in low- and high-velocity impacts), even for intact rock simulations, while, because of the second-order roughness of the rock due to its clastic nature, the impacts were oblique, resulting in the partition of the total kinetic energy. Energy losses, penetration depth, stress transmission through the rock mass, and the influence of the structural characteristics of the analogue rock were systematically investigated to provide some insights into the fundamental contributing mechanisms of impactor-fracture rock interactions.

Keywords PFC^{3D} · Collision · Proppant simulant · Fractured rock · Kinetic energy

Introduction

The interaction problem of proppant-proppant and proppant-rock systems has received a significant amount of research in petroleum geomechanics and engineering as it comprises a key constituent in the hydraulic fracturing stimulation in unconventional reservoir exploitation (Tomac and Gutierrez 2015; Ma et al. 2016; Wang and Sharma, 2018; Dong et al. 2019; Huang et al. 2020; Wang et al. 2019, 2020a; Zoback and Kohli 2019). Previous studies have examined the frictional problem of proppant-rock systems (Xiao et al. 2016; Zhang et al. 2019a, 2019b; He and Senetakis 2020; He et al. 2020), proppant damage and embedment (Ahamed et al. 2019; Bandara et al. 2018, 2020a, 2020b) as well as dynamic phenomena involved in rocks during the hydraulic fracturing process (Naghi Dehghan et al. 2014; Hadei and Veiskarami 2020; Li et al. 2021; Xu et al. 2021; Wang et al. 2021). As the analyses of proppant-rock (and proppant-fluid-rock) systems involve very complex mechanisms, researchers have attempted to examine the problem by means of discrete-based numerical simulations (DEM), coupled DEM with computational fluid dynamics (PFC-CFD) and finite element methods (PFC-FEM) as well as other numerical techniques (Zeng et al. 2016; Zhang et al. 2017, 2018, 2019c; Zheng and Tannant 2019; Hu et al. 2020; Li et al. 2020; Yang et al. 2020; Duan et al. 2018a, 2021). DEM (as well as DEM coupled with computational fluid dynamics codes) have also received a significant amount of research in the study of rock mechanics and fracture propagation problems (Duan and Kwok 2015; Duan et al. 2018b; Le et al. 2021; Peng et al. 2018, 2021, among others).

Most numerical studies examining the hydraulic fracturing process have investigated the performance of fractures in

✉ K. Senetakis
ksenetak@cityu.edu.hk

S. S. Kasyap
ssarvadev2-c@my.cityu.edu.hk

H. He
h_he@seu.edu.cn

[1] Department of Architecture and Civil Engineering, City University of Hong Kong, 83 Tat Chee Avenue, Kowloon, Hong Kong SAR

[2] Institute of Geotechnical Engineering, Southeast University, Nanjing 210096, China

Published online: 18 December 2021

the presence of proppants, fluid flow, crack propagation during hydraulic fracturing, and other essential aspects involved in unconventional reservoir analysis. However, the hydraulic fracturing process involves impacts among the proppants and between proppants and the rock. These processes may involve very complex mechanisms such as collision velocity influence, oblique impacts and damage development (Stronge 2018). Thus, fundamental studies of proppant-rock systems through collision experiments and simulations can provide additional insights into the behaviour of these complex systems, improving our understanding of the prevailing energy transport and dissipation mechanisms. Also, the presence of fractures or joints in the rock mass significantly alter their constitutive behaviour (Cui 2019; Jiang et al. 2017; Oh et al. 2017), which in turn becomes a concern for the associated impact mechanisms in the fractured rocks.

The collision (or impact) behaviour of solid objects, apart from its direct interest in the study of hydraulic fracturing problems, is also encountered in various industrial and natural systems, such as flow behaviour of powders and grains and pharmaceutical applications (Aryaei et al. 2010; Yu and Tafti 2016; Stronge 2018; Li et al. 2019), or granular flows and interactions of landslide materials with protective barriers (Iverson 1997; Clelland and Hrenya 2002; Moriguchi et al. 2009; Teufelsbauer et al. 2011; Cui et al. 2018; Hu et al. 2018; Jiang et al. 2018; Li and Zhao 2018; Shen et al. 2018; Tan et al. 2021; Yang et al. 2021). Within this context, many studies have attempted to provide fundamental insights into the impact problem of particle against block systems through experimental (Marinack et al. 2013; Patil and Higgs 2017; Tang et al. 2019; Wang et al. 2020b; Sandeep et al. 2020, 2021) and numerical simulations (Aryaei et al. 2010; Jiang et al. 2019; Tang et al. 2019; Wang et al. 2020b; Calvetti et al. 2017; Marzulli et al. 2020). An example of recent numerical simulation works highlighting the impact or collision behaviour of granular materials may refer in the study by Shen et al. (2019). In that work, the variation of contact forces, penetration and stress transmission due to the collision of a rock block of different shapes with a soil buffering layer were discussed. Also, Shen et al. (2017) studied the fragmentation process of rock due to impact loading using DEM simulations, and the influence of impact loading rate was explored. Other such works focussing on the impact problem in granular materials through discrete element methods include the studies by Bourrier et al. (2008) and Awasthi et al. (2015). On the other hand, both experimental and numerical works have been conducted to understand the behaviour of rocks (i.e. fracturing) due to impact loading (Wang and Tonon 2011; Chau et al. 2003; Giacomini et al. 2009), and these works classified the impact problem as a part of loading rate influences (e.g. Zhang et al. 2000). Loading rate influences have also been highlighted in previous fundamental studies in rocks mechanics examining the behaviour of fractures (e.g. Tang and Wong 2016); however, very limited number of numerical works are available discussing the impact behaviour of rock bed with pre-existing fractures and its influence on the impactor (e.g. Aziznejad et al. 2018).

The study of problems in hydraulic fracturing stimulation necessitates an understanding of the influence of pre-existing or newly developed fractures within the rock mass as well as other types of geological structures such as faults (Westwood et al. 2017; De Silva and Ranjith 2019a, 2019b; Ahamed et al. 2019; Duan and Kwok 2020; Li et al. 2020; Yang et al. 2020). Despite the significant amount of research on proppant-rock interactions, less attention has been given to the analysis of the influence of pre-existing fractures (or newly formed fractures) on the behaviour of the fundamental analogue system of single impactor colliding on rock base block, which may be additionally influenced by the velocity at collision (e.g. higher impact velocities may result in damage of the rock and inference of additional energy dissipation mechanisms). This problem, because of the clastic nature of many rocks involved in the hydraulic fracturing (such as mudrocks and siltstones), may result in second-order roughness, which may induce oblique impacts; oblique impacts influence the kinetic energy and the energy losses differentiating the behaviour of impactor-block systems significantly compared with that of direct impacts (Banks et al. 2005; Crüger et al. 2016; Higham et al. 2019).

In the present study, it was attempted to investigate the collision behaviour of an analogue proppant (impactor)-rock base system performing 3-dimensional discrete-based numerical simulations. The base block simulated in the study corresponds to a medium-strength clastic rock, and in the simulations, a pre-existing fracture of various geometries was considered. Major objectives of the present study were directed in the understanding of the influence of pre-existing fractures in the distribution of the total kinetic energy, the partition of translational and rotational components of kinetic energy and the role of the rock structural characteristics, as well as the variation of stresses within the rock (fractured) mass and the penetration of the impactor into the base, providing in this way some fundamental insights into the collision problem of proppant-rock systems. Even though major applications of the present study may be directed in the hydraulic fracturing stimulation (at the fundamental level of analogue single proppant–rock system), outcomes from the study may also find applications in other problems involving collisions of "particles" against fractured-cohesive systems.

Methodology

Three-dimensional (3D) DEM simulations were performed using the particle flow code (PFC) software to explore the behaviour of the impactor-base system under the influence of different fracture configurations in the base. The base

was modelled as a simulant of medium strength clastic rock using the bonded particle model, which, as a general contact model, has been adopted in many previous simulations of rock mechanics problems (e.g. Potyondy and Cundall 2004; Zhang and Wong 2014; Potyondy 2015; Peng et al. 2017, among others). In this study, the linear parallel bond contact model (Potyondy and Cundall 2004; Potyondy 2015) was implemented to simulate the cemented particles of the base, and a single rigid ball was modelled as the impactor colliding with the base (Fig. 1a). In the 3D linear parallel bond model, the force–displacement law for the bond force (normal and shear) and moment (twisting and bending) follows a linear trend and the bond breaks when the stresses (normal and shear) reach the limiting strength of the model. Equations (1) and (2) show the formulations for the normal stresses (which depend on the normal force and bending moment) and shear stresses (which depend on the shear force and twisting moment). Both the normal and shear stresses are updated at every cycle till the corresponding strength is reached.

$$\tilde{\sigma} = \frac{\overline{F}_N}{\overline{A}} + \overline{\beta}\frac{\|\overline{M}_B\|R}{\overline{I}} \tag{1}$$

$$\overline{\tau} = \frac{\|\overline{F}_S\|}{\overline{A}} + \beta\frac{\left|\overline{M}_T\right|R}{\overline{J}} \tag{2}$$

In Eqs. (1) and (2), F and M express forces and moments, respectively, and the subscripts N, S, B and T represent normal, shear, bending, and twisting directions, respectively. $\bar{A}$ represents the cross-sectional area, β represents the moment contribution factor (equal to 1 in the present study, after Potyondy 2011), R is the bond radius, I is the moment of inertia (bending direction), and J is the polar moment of inertia (twisting direction).

The analogue rock (base) was simulated as fractured, and a smooth joint contact model was applied to the desired range of balls depending on the width of the fracture to be simulated. The frictional joint behaviour was modelled for the fracture where the interface is linear-elastic and frictional (with the Coulomb limit for sliding). The Hertz contact model was assigned between the impactor and base block, where nonlinear formulations based on the theory of Mindlin and Deresiewicz (1953) were used to simulate the force–displacement behaviour. The force generated at a given contact is the algebraic summation of the nonlinear Hertz force and the dashpot force (with normal and shear components for both). The essential input parameters for the Hertz contact model in PFC are the effective shear modulus (G^*), the effective Poisson's ratio (υ^*), the friction coefficient (μ), the exponent (α) and the normal critical damping ratio (β_N). The calculation of the forces depends on these parameters and the surface gap (g_c) between the contacting bodies. Equations (3)–(5) show the formulations used in implementing the Hertz contact model in the PFC to estimate the normal forces using the mechanical properties and the displacements. The shear modulus values in Eq. (3) are calculated based on the elastic modulus and Poisson's ratio estimates. A low β_N (normal critical damping ratio) value of 0.1 was assumed between the impactor and the base block, representing a lower energy dissipation at the contact of the impactor and the base. The shear forces were calculated based on the initial values of normal force, shear force and tangential stiffness. A nominal friction coefficient of 0.1 was used between the impactor and the base rock. The simulations performed in the present study were direct impacts, in which case the major contribution of kinetic energy results from the vertical translational velocity (Z-axis).

$$F_N^H = -\frac{2G^*\sqrt{2R^*}}{3(1-\vartheta^*)}\left|g_c\right|^{\alpha} \tag{3}$$

$$F_N^D = (2\beta_N\sqrt{m_c k_n})\dot{\delta_N} \tag{4}$$

$$k_n = \alpha\frac{2G^*\sqrt{2R^*}}{3(1-\vartheta^*)}\delta_N^{\alpha-1} \tag{5}$$

The base block generated for these simulations was a 100-mm cube with spherical balls of radius 0.5 to 1.0 mm (total of 483,784 balls) and a density of 2600 kg/m^3. The impactor had a radius of 25 mm (0.25 times the base dimensions and 30 times the average ball size of the base) and a density equal to the base grains. Note that in these analyses, the critical factor to be simulated is, predominantly, not the absolute sizes of the impactor and the particles (or balls) of the analogue rock, but their relative size. For proppants corresponding to a mesh 40/70, the average size of the particles (or impactors) would be around 0.3 mm (after Bandara et al. 2020b), thus for proppants impacting on fine-grained siltstone (of 0.01 mm average size), the relative size of impactor over the rock grain size would be, approximately equal to 30.

To further understand the base rock behaviour in terms of its strength, a representative uniaxial compression strength (UCS) test was performed on the rock simulant in 3D PFC with the same micro-parameters as described in Table 1. UCS test was performed on a cylindrical sample of height at 100 mm and diameter at 50 mm, and the stress–strain variation was recorded during the simulation. Figure 1 b shows the UCS test sample and the fragments generated in the sample at the end of the test. The axial stress–strain variation during the UCS test is plotted in Fig. 1c. This analysis showed an unconfined compressive strength of 75 MPa and a strain at peak stress of around 0.06%. This compressive strength classifies the analogue rock simulated in the present

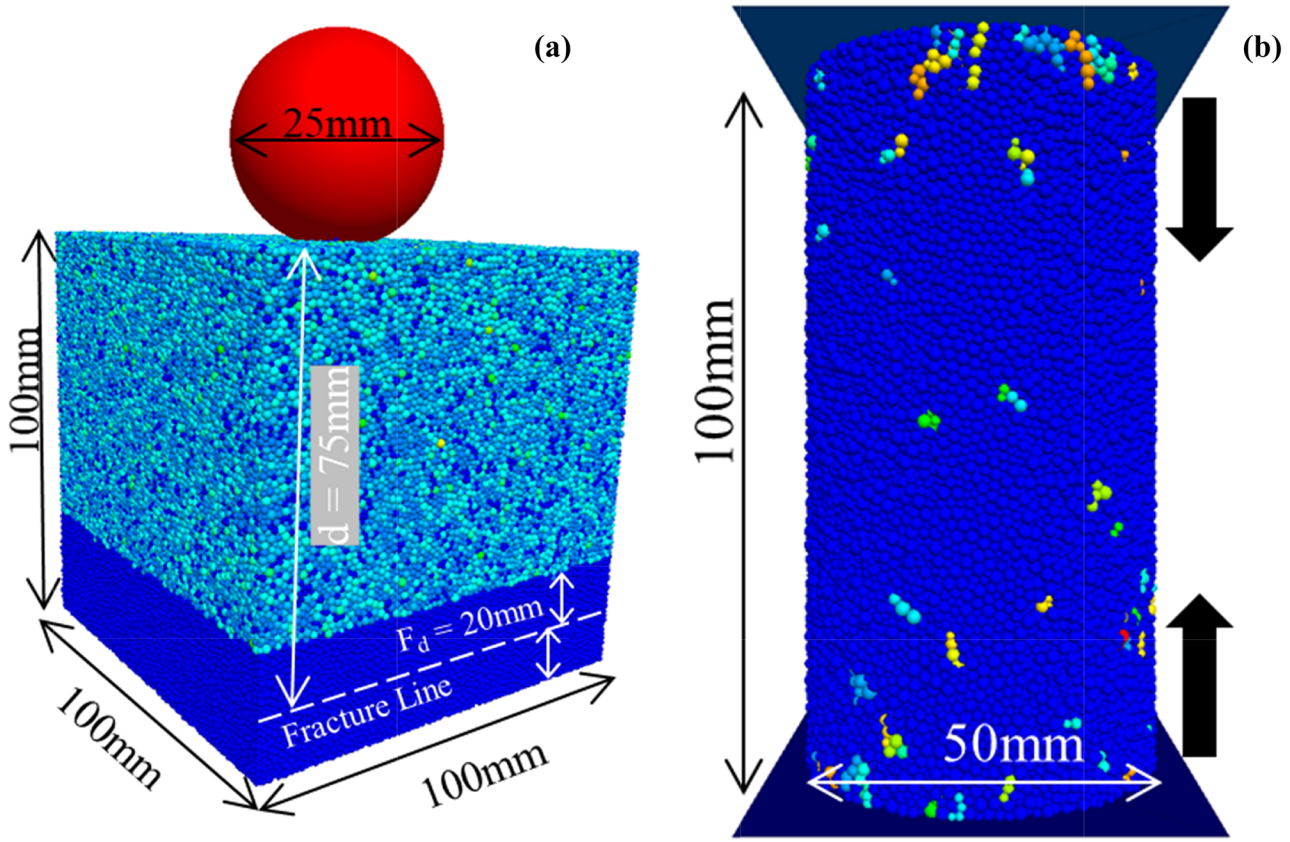
(a)
25mm
100mm
d = 75mm
F_d = 20mm
Fracture Line
100mm
100mm
(b)
100mm
50mm

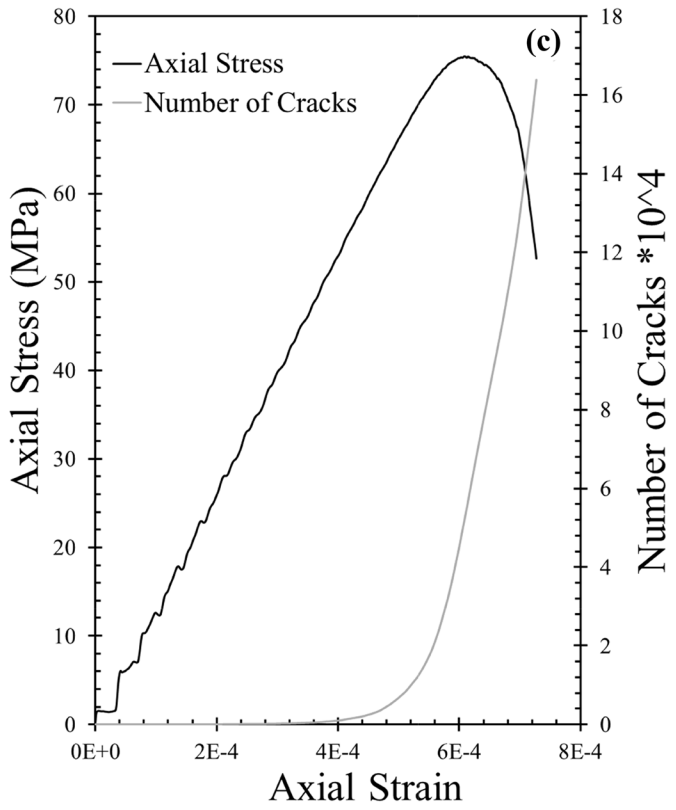
(c)
Axial Stress
Number of Cracks
Axial Stress (MPa)
Number of Cracks *10^4
Axial Strain
0E+0
2E-4
4E-4
6E-4
8E-4
0
10
20
30
40
50
60
70
80
0
2
4
6
8
10
12
14
16
18

◂**Fig. 1** Numerical setting: (**a**) 3D DEM model of rock base and impactor indicating different dimensions, (**b**) 3D DEM simulation of UCS test on the modelled rock simulant with fragments (each colour stands for different fragment: 258 fragments were generated at peak stress), (**c**) axial stress–strain variation and the number of cracks generated in the sample

study as a medium-strength material, according to ISRM suggestions (Clout and Manuel 2015). Figure 1 c also shows the number of fractures developed in the rock during the UCS test, further signifying the weaker strength of the bond between the grains in the rock.

The fracture properties were set to represent frictional joints with zero cohesion and zero tensile strength. Other details of the input parameters for the impactor, the base, and the fracture used in the present simulations are shown in Table 1. In this study, only horizontal fractures were simulated in the base i.e. the normal of the fracture plane and the initial kinetic energy of the impactor are in the Z-direction. The primary intention of the present study is to understand the impactor behaviour upon colliding with the rock base, and hence the microparameters used in the present 3D model were arbitrarily chosen based on the previous micromechanical experiments of the authors (Kasyap and Senetakis 2020; Kasyap et al. 2021). Particularly, the impact calibration parameters (i.e. the contact properties between the impactor and the base) were meticulously selected based on impact experiments and tribological micromechanical-based tests (Sandeep et al. 2020, 2021; Sandeep and Senetakis 2018, 2019).

A parametric study was conducted by simulating collisions by varying the impactor velocity, fracture width and fracture depth from the surface. The influences of two impact velocities ($V_i = 1$ m/s and 10 m/s), three fracture widths ($F_d = 0.2$ mm, 2 mm and 20 mm) representing extremely close spacings in accordance with the international rock classification system (ISRM 1978, after Sivakugan et al. 2013), and two fracture distances from the impact surface ($d = 25$ mm and 75 mm) were systematically studied. The present 3D base block model has a total number of contacts (parallel bonded) of more than three million with a bond coordination number of around 11. For the three cases of fracture widths, the total number of contacts involved in the fracture are 1%, 4.7%, and 41% for $F_d = 0.2$ mm, 2.0 mm and 20 mm, respectively. Note that the fracture distances from the rock surface correspond to one and three times the size of the colliding impactor, thus representing near-surface fractures based on the relative dimensions of the problem.

Table 1 Parameters for 3D-DEM model

Property description		Base block
Particles (balls)	Ball radius (mm)	0.5–1.0 (average: 0.75)
	Normal to shear stiffness ratio	2.5
	Coefficient of friction	0.5
	Density (kg/m^3)	2600
	Young's modulus (GPa)	60.0
Parallel bond	Model	Linear parallel bond
	Young's modulus (GPa)	60.0
	Tensile strength (MPa)	10
	Cohesion (MPa)	50
	Normal to shear stiffness ratio	2.5
Impactor	Contact model with base	Hertz
	Ball radius (mm)	25
	Effective shear modulus (GPa)	28
	Normal critical damping ratio	0.1
	Poisson ratio	0.25
	Friction coefficient	0.1
Fracture properties	Model	Smooth joint
	Size (m)	0.15
	Distance from impacting surface (m)	0.025, 0.075, Inf
	Fracture width (mm)	0.2, 2.0, 20.0
	Friction coefficient	0.7
	Normal Stiffness (GPa/m)	2.0
	Shear stiffness (GPa/m)	3.0
	Cohesion (MPa)	0.0
	Tension (MPa)	0.0

These results were compared with the behaviour of the intact base (no fracture case). A total of 14 different numerical simulations were performed, and parameters such as the total kinetic energy (KE) of the impactor (and its partitions), the penetration of the impactor into the base upon collision, the number of contacts made by the impactor with the base, the contact forces generated in the impactor and the transmission of stress waves in the base block are examined in this study. The penetration distance of the impactor is calculated as the change in vertical position of the impactor from the point of first contact to the point of rebound initiation.

Results and discussion

Kinetic energy and its partitions

The variations of the total kinetic energy (KE) of the impactor (three translational and three rotational components) with time during the impact and rebound phases are shown in Fig. 2. The curves were plotted based on the time duration between the first contact of the impactor with the base to its final contact. The influence of impact velocity (V_i), fracture width (F_d) and fracture distance (d) are compared in this figure. The no-fracture cases ($d = Inf$) are plotted in all the respective sub-figures at $V_i = 1$ m/s and 10 m/s for comparison with $d = 25$-mm and 75-mm cases for different fracture widths. For low-velocity impact, the kinetic energy versus time variation was similar for $d = Inf$ and $d = 75$-mm cases, and only slight additional energy losses (20% more than the no-fracture case) were observed with $F_d = 20$ mm. However, for the nearest surface fracture ($d = 25$ mm), the energy losses increased significantly with increasing fracture width, implying that the collision behaviour of the impactor-block system is highly sensitive to small changes of the fracture distance from the surface i.e. a distance of one or three times the impactor diameter results in a substantial difference in the energy losses. The numerical data of the near-surface fracture cases also suggested that the total duration of the impact process was doubled when the fracture size increased from 0.2 to 20 mm for low-velocity impact. For high-velocity impact, the increase was even higher. Due to the presence of a fracture near to the surface, the effective resistance from the base to the impactor will be significantly low, leading to deeper penetrations (discussed in subsequent section). Hence, the total time duration between the start of the impact and the end of the rebound is higher for near-surface wide fractures.

For 10-m/s impacts, there were observed significant energy losses due to the collision in all the cases of fracture widths and distances as there was extensive breakage of the contact bonds in the base block, unlike the low-velocity impact. Hence, some oscillations in the kinetic energy versus time curves (Fig. 2) were observed owing to the large number of contacts made with the base grains (discussed in "Penetration and contacts of the impactor") and the bonds broken during the impact. In the ideal case of no-fractures in the base block (i.e. intact rock), with one order higher impact velocity, the coefficient of restitution of the impactor substantially decreased from 0.867 at 1-m/s impact velocity, to 0.091 at 10-m/s impact velocity (note that the coefficient of restitution from the simulations at low-velocity impacts would match the general range of values reported by Sandeep et al. (2021), on perfect sphere-stiff block collision experiments). In the high-velocity impacts, approximately 90% of the impactor energy was absorbed by the base block caused, predominantly, by the bond breakage. Further discussion of the differences in energy for the impacts at lower and higher velocities is discussed in "Contact force of the impactor and normal stress in the base".

In the case of low-velocity impacts, the energy loss was highest for the nearest-surface fracture, as most of the energy was absorbed by the fracture plane without much energy return to the surface. Also, as the fracture width increased, the rebound energy decreased, and the contact duration increased. However, with high-velocity impacts, the kinetic energy variation and hence the impact behaviour was different for different fracture widths. At $F_d = 0.2$ mm, the fracture nearest to the surface ($d = 25$ mm) showed a higher energy loss similar to the low-velocity impact. However, as the fracture width increased to 2 and 20 mm, the total kinetic energy (KE) of the impactor was the highest with near-surface fracture, and the COR (coefficient of restitution) increased with increasing fracture width (from 0.114 at $F_d = 2.0$ to 0.383 at $F_d = 20$ mm). This increased COR or decreased energy losses with larger-in-width fractures in high-velocity impacts is possibly contributed by the additional resistance from the disruption of the fracture zone. An example of such disruption of the base in the present DEM simulations is shown in Fig. 3a. However, the contact time has increased significantly due to the extensive embedment of the impactor into the rock base. The interpretations made from the disruption condition in the base block as shown in Fig. 3a are compared with an example of fracture configuration with lower vulnerability (i.e. $V_i = 10$ m/s, $F_d = 20$ mm, $d = 75$ mm, Fig. 3b). The post-impact behaviours of the base block with near- and far-surface fractures at the same impact velocity and fracture width are extremely different. The disruption phenomenon observed in the near-surface fracture case was not observed and only a slight crater formation was noticed at the impact location. However, the key observation to be made is the COR values in order to quantitatively evaluate the influence of disruption in the base block. As previously discussed in this section, higher COR is observed when the base block is disrupted due to the impact, as additional resistances induce greater rebound kinetic energy to the impactor. This

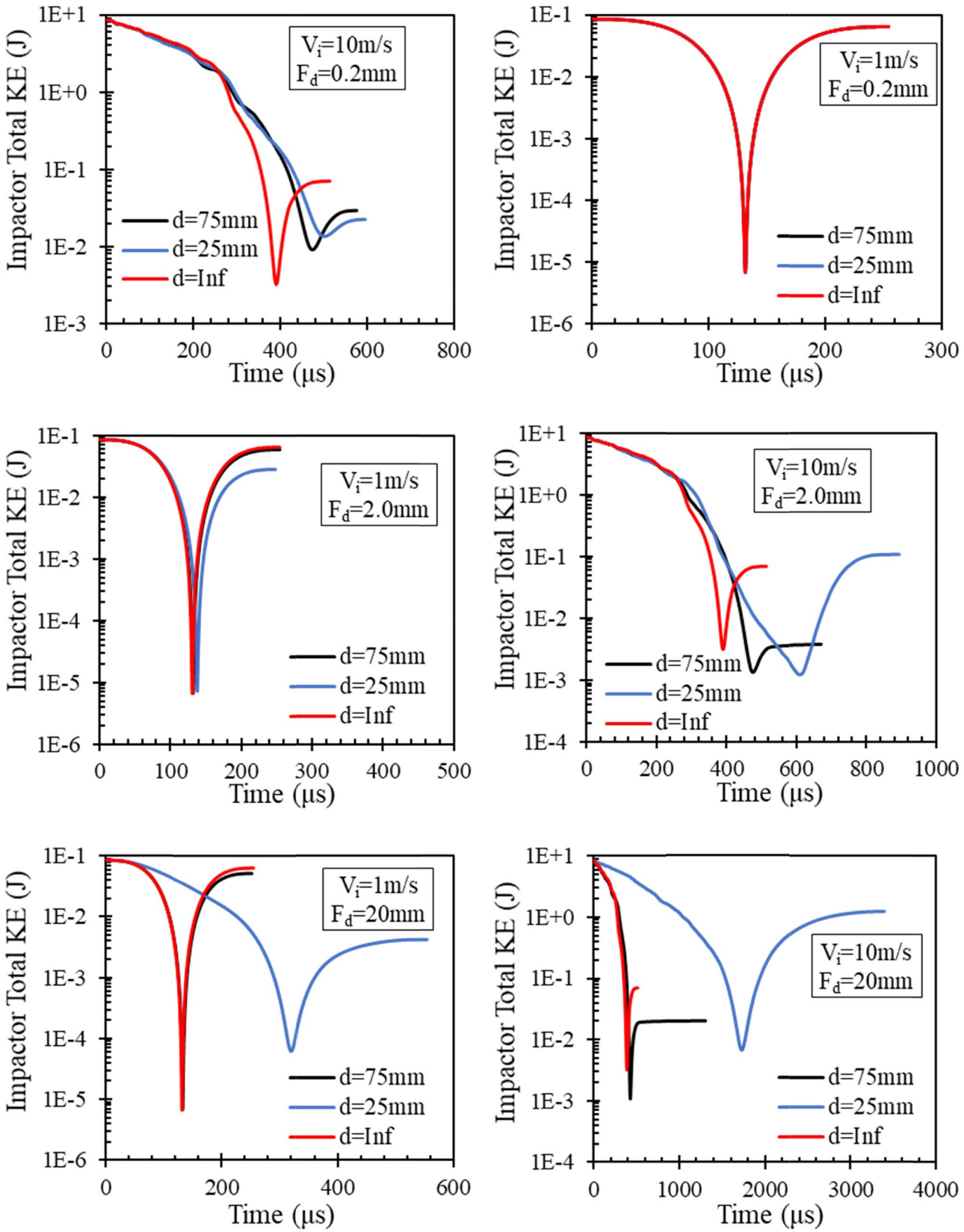

Fig. 2 Variation of total kinetic energy of the impactor at different impact velocities and fracture distances

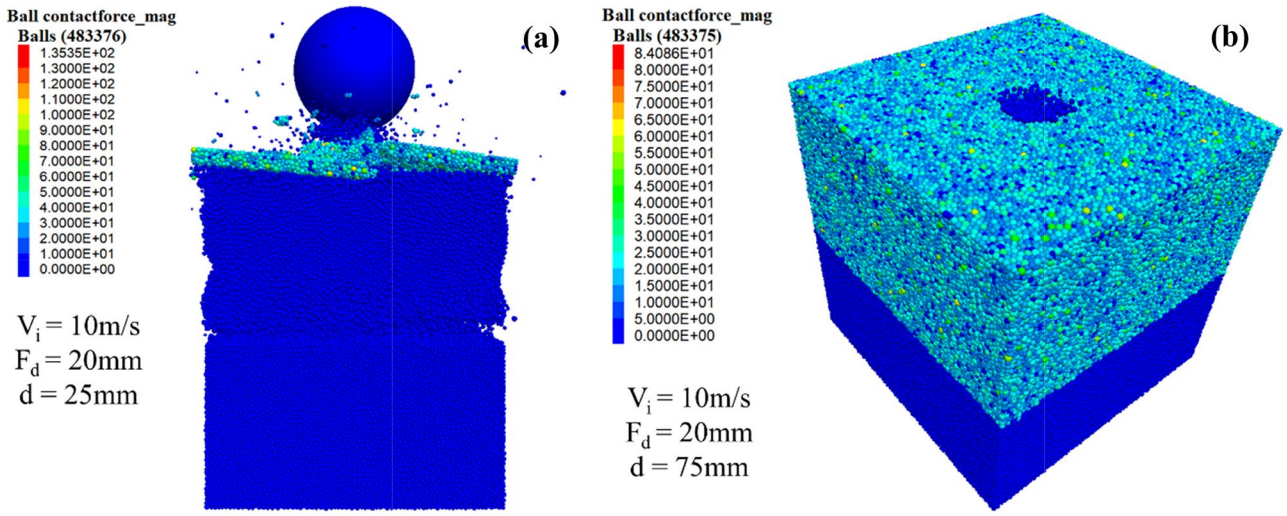

Fig. 3 Behaviour of base block upon impact at $V_i = 10$ m/s with $F_d = 20$ mm at **a** $d = 25$ mm and **b** $d = 75$ mm. Legends represent the contact force magnitude of the balls in N

additional resistance to the impactor is possibly generated from the kinetic energy of the grains in the base block tending to move at different velocities (predominantly vertically away from the base) due to the disruption. In the case as shown in Fig. 3b with no disruption, the COR of the impactor was lower than 0.05 i.e. at least 7.5 times lower for far-surface fracture than the near surface fracture.

At both low and high-velocity impacts, it was observed that the kinetic energy of the impactor has never reached zero for all the cases of fracture widths and distances. This is because at least one of the impactor velocity components is a nonzero value when the dominant vertical translational kinetic energy (TKE-Z) is zero. This transition of initial TKE-Z to other components after the impact is due to the localized obliqueness at the impact location (Fig. 4a), while the global behaviour is a direct impact with the angle between the impactor kinetic energy vector and the normal vector of the base block (as a whole) to be equal to zero. When the impactor collides with the base, different sizes of base grains oriented in various directions within the impact zone and the sliding friction at the impactor contact lead to the transfer of initial TKE-Z into other translational and rotational components. The total kinetic energy of the impactor at any point in the impact process can be divided into three translational velocities (TKE-X, -Y and -Z) and three rotational velocities (RKE-X, -Y and -Z). At the maximum point of penetration i.e. when TKE-Z is zero, the percentages of the other five kinetic energy components are quantified and their variation is plotted in Fig. 4b, c for all the simulation cases. Though the absolute values of these five KE components (other than TKE-Z) are smaller than the dominant TKE-Z, it provides a basis for the conception of impactor behaviour due to the fractures.

It is to be noted that the present study describes the behaviour for one particular case of local oblique and global direct impact. This localized oblique impact in the present DEM model due to the scale of the contacting grains can be comprehended on a larger scale as the result of mesoscale roughness of the rock surface (second order roughness), which is controlled by the undulation due to the clastic texture of the rock. With random arrangements of grains in the base, the numerical values of the energy partitions might be different but the tendencies of the impactor to rotate and spin are highly dependent on the fracture configurations and impact velocities. A more systematic analysis would be required to correlate the kinetic energy partitions and bond arrangement, which is beyond the scope of the present study.

The partitions of kinetic energies were entirely different at the two impact velocities. For low-velocity impact (1 m/s), there was no significant influence of the fracture width when the fracture is farther from the impact surface ($d = 75$ mm), with most of the kinetic energy to correspond to rotational component (around 76%). When the fracture is nearer at the surface, this propensity of the impactor to slide is dependent on the fracture width, possibly caused by the greater number of broken contacts. On the other hand, with the high-velocity impacts (10 m/s), the impactor showed an increasing tendency to slide than to spin as the fracture width increased from 0.2 to 20 mm. It can be comprehended that a larger fracture width (comparable with the size of the impactor) tends to disrupt the kinetic energy of the impactor caused by the significant damage of the base block. When this damage is magnified with nearer-surface fractures, the behaviour becomes highly erratic, demonstrating the high complexities in the hydraulic fracturing stimulation of proppant-rock interactions (as well as other problems involving collisions)

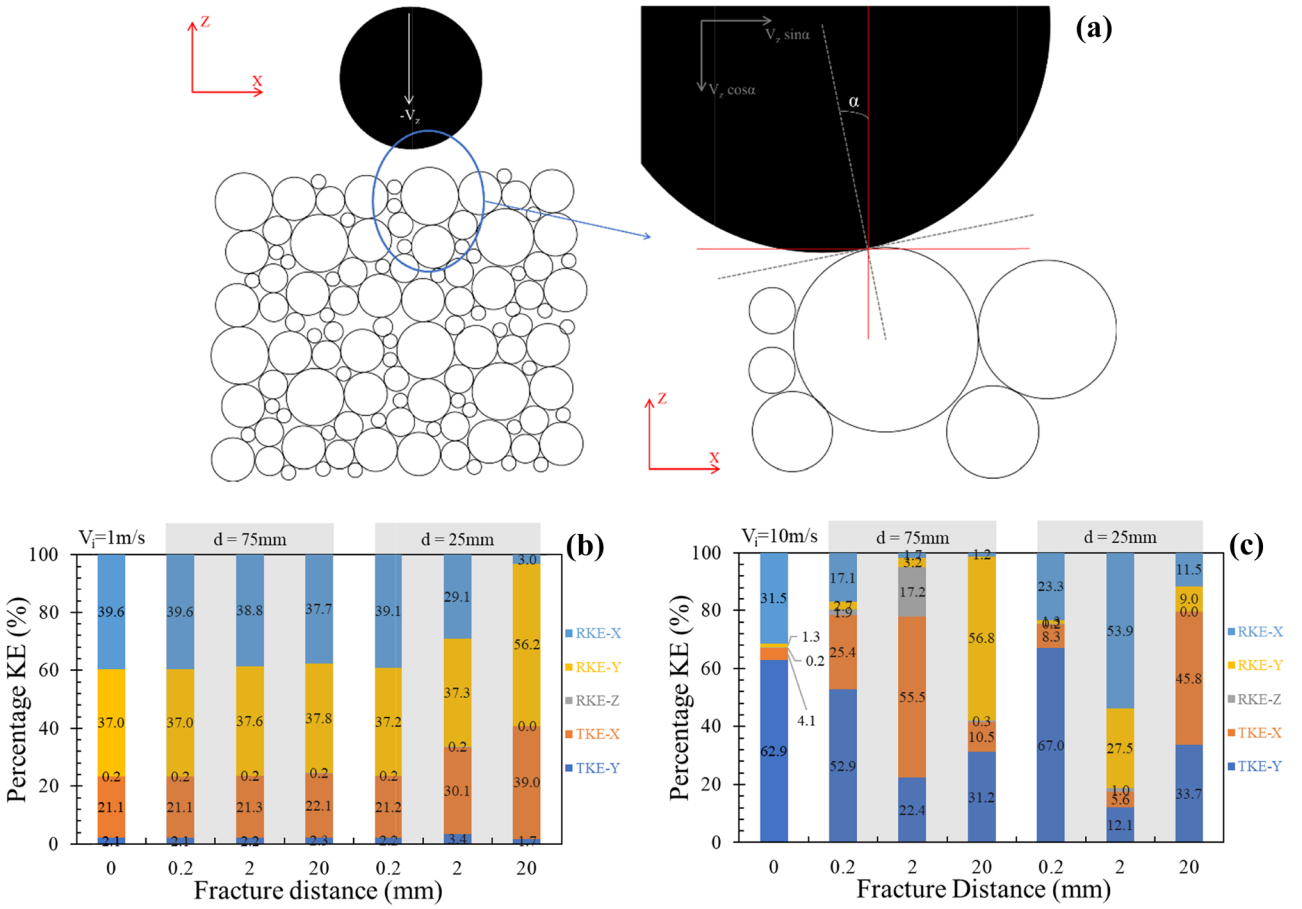

Fig. 4 Analysis of the kinetic energy and obliqueness of the impacts: **a** schematic description of localized oblique impact in the DEM simulations. Partitions of kinetic energies (translation and rotation) at zero translational kinetic energy in the impact direction for **b** low-velocity impact and **c** high-velocity impact

and the sensitivity of the geometry of the problem i.e. fracture geometry, its distance from the rock surface, the impact velocity, among other factors.

Penetration and contacts of the impactor

During the impact phase, the impactor penetrates the base block as the TKE-Z in its kinetic energy is a dominant component. This penetration is critical in understanding the crater depths and the corresponding damages induced in the rock mass and granular media in various impact problems (Suzuki et al. 2012; Melosh and Collins 2005; Uehara et al. 2003; Walsh et al. 2003). The impact velocity is known to be one of the critical factors for the penetration depth variation. The following discussions report the variation of penetration depth at different impact velocities under the influence of fracture in the base block. Figure 5 compares the variation of penetration depth of the impactor in different impact simulations. These variations are compared with the corresponding number of contacts made by the impactor, evaluating the compaction and acceleration mechanisms in the impact phase of the simulation.

The primary difference observed between the low and high-velocity impacts in the present simulations was the mode of penetration. In low-velocity impacts, even with the gravest fracture conditions ($d = 25$ mm and $F_d = 20$ mm), the impactor rebounded without damaging the surface, as observed from the positive values of penetrations in Fig. 5. For the rock base, due to its particle size (in the range of 0.5–1 mm), some protrusions occurred beyond the size of the block, and the impact phase was completed solely by contacting the surface grains of the block. As can also be observed from the number of contacts (N_c = number of balls in the base contacted by the impactor) shown in Fig. 5, the maximum N_c value for $V_i = 1$ m/s was 4. The maximum penetration was observed for the most adverse fracture configuration ($d = 25$ mm and $F_d = 20$ mm), and the absolute value of penetration (or displacement) was 0.177 mm ($N_c = 3$), which is only 24% of the average ball radius of the base block. For $V_i = 10$ m/s, the impactor penetrated around

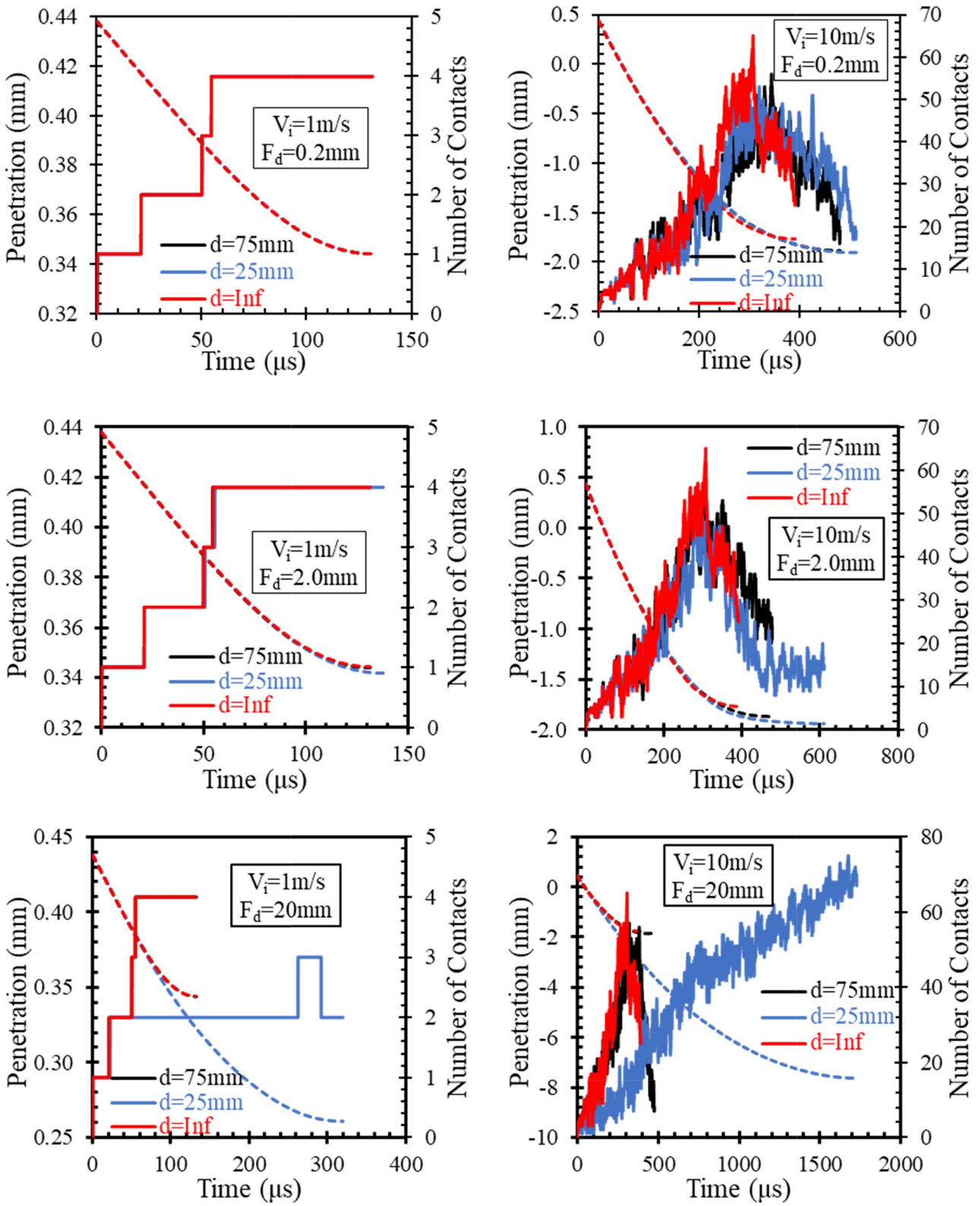

Fig. 5 Variation of penetration of the impactor into the base at different impact velocities and fracture configurations. (The dotted lines indicate penetration and the solid lines indicate number of contacts)

1.8 mm into the base block (total penetration of 2.2 mm) for the case without fracture. Only minute changes in penetration (and the corresponding time) were observed with the $d = 75$ mm case, but the $d = 25$-mm case showed significant penetration when the fracture width was 20 mm. This behaviour was similar to the low-velocity impact case but with around 30 times higher magnitude of penetration. The N_c variation also showed values around one order of magnitude higher than the low-velocity impact, and the values were highly irregular during the impact phase.

Another primary difference between low and high-velocity impacts is the number of contacts at the maximum penetration point. Irrespective of the number of contacts, the low-velocity impacts showed the highest N_c value at the maximum penetration point. On the other hand, the high-velocity impacts showed a significant drop in the number of contacts before the maximum penetration as numerous bonds were broken and lost contact with the impactor. This behaviour will be reflected in the contact force of the impactor (discussed in "Contact force of the impactor and normal stress in the base"). A combined observation of N_c and penetration depth variations indicates that in the initial stages of the impact phase, the impactor penetrates into the base by making more contacts (increasing N_c), and then the stiffness between the impactor and the already contacted base grains (stable N_c) prevents (instantly) further penetration to reach the maximum point. The fraction of time in the impact phase (from the first contact with the base to zero kinetic energy of the impactor) increases with increasing fracture width (from no fracture to $F_d = 20$ mm). This behaviour was evident for 1-m/s impacts, but the higher impact velocity showed an irregular trend as the number of contacts made by the impactor are oscillating. For $F_d = 2.0$ mm and 20 mm at $V_i = 10$-m/s case, a slight indication of stable N_c can be observed from the horizontal variation and change in the slope of N_c versus time curves, respectively. This phenomenon abstractedly describes the resistance from the base block to the generation of macroscopic changes (which can be understood from the rapidly changing N_c).

Contact force of the impactor and normal stress in the base

"Kinetic energy and its partitions" and "Penetration and contacts of the impactor" discussed the variation of the impactor-rock interaction at two collision velocities under the influence of different base block fracture configurations. Once the impact occurs, stress waves transmit through the base block and based on the energy absorbed by the base block, the rebound characteristics of the impactor vary (considering completely rigid impactor). A two-dimensional DEM study by Aziznejad et al. (2018) showed that the stress waves transmitting in the rock originated from an impact on its surface can reflect at the joint and modify the damage configuration of the rock. They also concluded that the cracks generated in the rock due to the impact stop at the fracture and are orthogonal to the fracture. In this section, the variation in the stresses recorded at the bottom end of the base block upon impact is analysed, and the effects of different fracture configurations are highlighted. These variations of stresses are correlated with the contact force of the impactor to highlight the influence of the fracture. A measurement region of 5-mm radius was created at the bottom end of the base block, and the normal stresses, both vertical and lateral i.e. parallel and perpendicular to the impact direction, respectively, were recorded in that region.

In Fig. 6, the stresses (both vertical and lateral) generated at the bottom centre of the base rock are plotted for selected cases to delineate the behaviour. When the base rock is intact (without any fractures), the average stresses in the measured region varied significantly with the impact duration. The tensile lateral stresses and the compressive normal stresses were highest when the impactor contact force was at its peak. Due to the presence of fracture, the stress waves were delayed reaching the bottom of the base block, and the delay was higher with larger fracture width. When the fracture is farther from the impact surface ($d = 75$ mm), the delay was even higher, and the intensity of the stress waves (relatable with the normal stresses) was reduced due to the dissipation of energy at the bonds above the fracture. The peak values of the stresses in the base block were attained after the completion of the impact process (impact and rebound), as indicated by the dotted lines in Fig. 6. Also, significant undulations in the stresses were observed only when the fracture was nearest to the surface (or farthest from the measuring region). This phenomenon can be attributed to the multiple reflections and refractions of the stress waves originating from the vibration of the bonded grains. One such simple observation can be derived from the case of $V_i = 1$ m/s with $F_d = 20$ mm and $d = 25$ mm (near surface) where two peaks in the normalized impactor contact force variation were observed. When the impactor contact force variation in Fig. 6 is correlated with the number of contacts variation in Fig. 5, the horizontal segment in N_c associated with increased penetration led to the drop in the impactor contact force and a new contact developed during the final stage of the impact phase which led to an additional peak in the impactor contact force. This particular example is a simple observation to relate the number of contacts and the contact force of the impactor, and this phenomenon is intensified in the high velocity impacts (10 m/s). On the other hand, when the fracture is closer to the base, these reflections and refractions are filtered by the loosely packed fracture zone grains, and the stresses recorded below the fracture zone are comparatively regular. It was also observed that the vertical stresses were also in the compressive mode, while the lateral stresses oscillated at different magnitudes and frequencies in compressive and

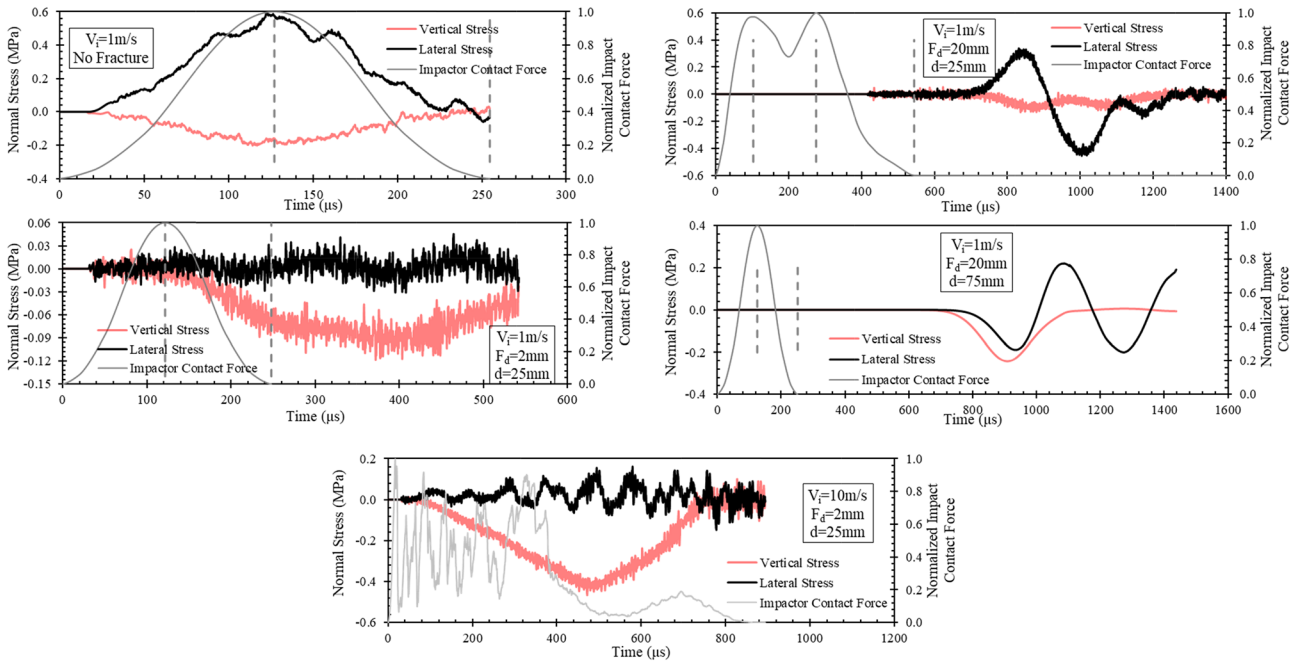

Fig. 6 Variation of vertical and lateral stresses at the bottom of the base due to the impact on the top surface under different impact velocities and fracture configurations

tensile modes. This oscillation of lateral stresses was dominant at high-velocity impacts. One particular example of $F_d = 2$ mm and $d = 25$ mm at $V_i = 10$ m/s is shown in Fig. 6. The phenomenon of delayed stress wave arrivals due to a fracture holds good also for high-velocity impacts. The variation of the normalized impactor contact force in high-velocity impacts is irregular with time unlike the low-velocity impacts, while the stresses in the base block are harmonically varying with time in both the cases. Despite the irregularities in the high-velocity impacts, the maximum value of impactor contact force was before the arrival of stress waves to the base of the block. Since the number of contacts made by the impactor with the grains of the base is significantly high (as discussed in "Penetration and contacts of the impactor"), there exists multiple origins of stress waves from the contact between impactor and base, and also internal reflections of these stress waves are predominant.

Conclusions

Three-dimensional DEM simulations were performed on impactor-block systems to conduct a systematic parametric study exploring the influence of a horizontal fracture in a rock on the impact behaviour of the system. Two impact velocities, three fracture widths and two fracture distances from the impact surface were simulated, and the corresponding behaviour of the impactor and the base block was compared with intact base block condition. The base block represented an analogue medium-strength clastic rock, and the linear parallel bond contact model was implemented to simulate the cemented rock particles. The following major conclusions were drawn from the simulation test results.

1) The presence of fractures in the base rock primarily resulted in increased impact duration (impact and rebound phase), and the variation was significantly higher when the fracture was nearer to the surface. The loss of kinetic energy of the impactor was higher with graver fracture configurations (larger width and nearer to the surface), but an opposite trend was observed with high-velocity impact where additional kinetic energy was appended to the impactor due to the disruption of the base block.
2) For the nearest surface fracture (distance from the rock free surface equal to the impactor size), the energy losses increased significantly with increasing fracture width, implying that the collision behaviour of the impactor-block system is highly sensitive to small changes in the fracture distance from the surface i.e. a distance of one or three times the impactor diameter resulted in a substantial difference in the energy losses.
3) A trend between the penetration of the impactor and the number of contacts made with the base block delineated the compaction and acceleration phenomena of the impactor during the impact phase. The penetration

depths were higher for the nearer-surface fractures and the penetration magnitude increased with the fracture width.

4) At the maximum penetration depth and when the translational kinetic energy in the vertical direction (TKE-Z) became zero, the fractions of other kinetic energy components (translation and rotational in different directions) for low-velocity impacts systematically varied with different fracture configurations. With the fractures nearer to the surface, the rotational kinetic energy decreased and the translational kinetic energy increased as the fracture width increased, signifying a sliding tendency of the impactor.
5) The stress transfer within the base block due to the impact was delayed due to the fracture in the base block. As the fracture width increased, the delay in the arrival of the stress waves to the bottom of the base from the impact location increased. This delay was found to be greater than the whole impact duration. When the fracture was closer to the impact location, higher noise in the stresses was observed owing to the significant internal reflections.

Funding The work described in this article was fully supported by the grants from the Research Grants Council of the Hong Kong Special Administrative Region, China, Project No. "CityU 11210419" and Project No. "CityU 11214218" and an SRG-Fd Grant from City University of Hong Kong, Project No. "7005670".

References

Ahamed MAA, Perera MSA, Dong-yin Li, Ranjith PG, Matthai SK (2019) Proppant damage mechanisms in coal seam reservoirs during the hydraulic fracturing process: a review. Fuel 253:615–629

Aryaei A, Hashemnia K, Jafarpur K (2010) Experimental and numerical study of ball size effect on restitution coefficient in low velocity impacts. Int J Impact Eng 37:1037–1044

Awasthi A, Wang Z, Broadhurst N, Geubelle P (2015) Impact response of granular layers. Granular Matter 17:21–31

Aziznejad S, Esmaieli K, Hadjigeorgiou J, Labrie D (2018) Responses of jointed rock masses subjected to impact loading. J Rock Mech Geotech Eng 10(4):624–634

Bandara KMAS, Ranjith PG, Rathnaweera TD, Perera MSA, Kumari WGP (2018) Thermally-induced mechanical behaviour of a single proppant under compression: insights into the long-term integrity of hydraulic fracturing in geothermal reservoirs. Measurement 120:76–91

Bandara KMAS, Ranjith PG, Rathnaweera TD (2020a) Laboratory-scale study on proppant behaviour in unconventional oil and gas reservoir formations. J Nat Gas Sci Eng 78, 103329.

Bandara KMAS, Ranjith PG, Rathnaweera TD, Wanniarachchi WAM, Yang SQ (2020b) Crushing and embedment of proppant packs under cyclic loading: an insight to enhanced unconventional oil/gas recovery. Geosci Front [Published online]. https://doi.org/10.1016/j.gsf.2020.02.017.

Banks M, Bridges NT, Benzit M (2005) Measurements of the coefficient of restitution of quartz sand on basalt: implications for abrasion rates on earth and mars. 36th Annual Lunar and Planetary Science Conference 2116.

Bourrier F, Nicot F, Darve F (2008) Physical processes within a 2D granular layer during impact. Granular Matter 10:415–437

Calvetti F, di Prisco CG, Vairaktaris E (2017) DEM assessment of impact forces of dry granular masses on rigid barriers. Acta Geotech 12:129–144

Chau KT, Wu SZ, Zhu WC, Tang CA, Yu TX (2003) Dynamic fracture and fragmentation of spheres. 16th ASCE Engineering Mechanics Conference, Seattle.

Clelland R, Hrenya CM (2002) Simulations of a binary-sized mixture of inelastic grains in rapid shear flow. Phys Rev E 65(3):031301. https://doi.org/10.1103/PhysRevE.65.031301

Clout JMF, Manuel JR (2015) Minerology, chemical, and physical characteristics of iron ore Iron Ore, Woodhead Publishing 45–84. https://doi.org/10.1016/B978-1-78242-156-6.00002-2

Crüger B, Heinrich S, Antonyuk S, Deen NG, Kuipers JAM (2016) Experimental study of oblique impact of particles on wet surfaces. Chem Eng Res Des 110:209–219

Cui Y (2019) Effect of joint type on the shear behavior of synthetic rock. Bull Eng Geol Environ 78:3395–3412

Cui Y, Choi CE, Lui LHD, Ng CWW (2018) Effects of particle size of mono-disperse granular flows impacting a rigid barrier. Nat Hazards 91:1179–1201

De Silva VRS, Ranjith PG (2019a) Intermittent and multi-stage fracture stimulation to optimise fracture propagation around a single injection well for enhanced in-situ leaching applications. Eng Fract Mech 220, 106662.

De Silva VRS, Ranjith PG (2019b) Evaluation of injection well patterns for optimum fracture network generation host-rock formations: an application in in-situ leaching. Miner Eng 137:319–333

Dong KJC, He WH, Wang M (2019) Effect of surface wettability of ceramic proppant on oil flow performance in hydraulic fractures. Energy Science and Engineering 7(2):504–514

Duan K, Kwok CY (2015) Discrete element modeling of inherently anisotropic rock under Brazilian test conditions. Int J Rock Mech Min Sci 78:46–56

Duan K, Kwok CY, Wu W (2018a) DEM modeling of hydraulic fracturing in permeable rock: influence of viscosity, injection rate and in-situ states. Acta Geotech 13(5):1187–1202

Duan K, Wu W, Kwok CY (2018b) Discrete element modelling of stress-induced instability of directional drilling boreholes in anisotropic rock. Tunn Undergr Space Technol 81:55–67

Duan K, Kwok CY (2020) On the initiation, propagation and reorientation of simultaneously-induced multiple hydraulic fractures. Computers and Geotechnics 117, 103226.

Duan K, Li Y, Yang W (2021) Discrete element method simulation of the growth and efficiency of multiple hydraulic fractures simultaneously-induced from two horizontal wells. Geomech. Geophys. Geo-energ. Geo-resour. 7(3). https://doi.org/10.1007/s40948-020-00196-4.

Giacomini A, Buzzi O, Renard B, Giani GP (2009) Experimental studies on fragmentation of rock falls on impact with rock surfaces. Int J Rock Mech Min Sci 46:708–715

Hadei MR, Veiskarami A (2020) An experimental investigation of hydraulic fracturing of stratified rocks. Bull Eng Geol Env 80:491–506

He H, Luo L, Senetakis K (2020) Effect of normal load and shearing velocity on the interface friction of organic shale – proppant simulant. Tribol Int 144:106119. https://doi.org/10.1016/j.triboint.2019.106119.144,106119

He H, Senetakis K (2020) A micromechanical study of shale rock-proppant composite interface. J Petrol Sci Eng 184:106542. https://doi.org/10.1016/j.petrol.2019.106542

Higham JE, Shepley P, Shahnam M (2019) Measuring the coefficient of restitution for all six degrees of freedom. Granular Matter 21(15). https://doi.org/10.1007/s10035-019-0871-0.

Hu J, Li L, Shi S, Zhou Z, Liu H, He P (2018) Field, experimental, and numerical investigation of a rockfall above a tunnel portal in southwestern China. Bull Eng Geol Env 77:1365–1382

Hu Y, Li X, Zhang Z, He J, Li G (2020) Numerical investigation on the hydraulic stimulation of naturally fractured Longmaxi shale reservoirs using an extended discontinuous deformation analysis (DDA) method. Geomech. Geophys. Geo-energ. Geo-resour. 6(73). https://doi.org/10.1007/s40948-020-00195-5.

Huang H, Babadagli T, Li H, Develi K, Zhou D (2020) A visual experimental study on proppants transport in rough vertical fractures. Int J Rock Mech 134, 104446.

ISRM, International Society for Rock Mechanics (1978) Suggested methods for quantitative description of discontinuities in rock masses. International Journal of Rock Mechanics and Mining Sciences & Geomechanics Abstracts 15(6):319–368

Iverson RM (1997) The physics of debris flows. Rev Geophys 35(3):245–296. https://doi.org/10.1029/97RG00426

Jiang M, Liu J, Crosta GB, Li T (2017) DEM analysis of the effect of joint geometry on the shear behavior of rocks. Comptes Rendus Mécanique 345(11):779–796

Jiang S, Shen L, Guillard F, Einav I (2018) Energy dissipation from two-glass-bead chains under impact. Int J Impact Eng 114:160–168

Jiang Z, Du J, Rieck C, Bück A, Tsotsas E (2019) PTV experiments and DEM simulations of the coefficient of restitution for irregular particles impacting on horizontal substrates. Powder Technol 360:352–365

Kasyap SS, Senetakis K (2020) An experimental investigation on the tribological behaviour of quartz grains with dry to saturated gouge material. Pure Appl Geophys 177:3283–3300

Kasyap SS, Senetakis K, Coop MR, Zhao JD (2021) Micromechanical behaviour in shearing of reproduced flat LBS grains with strong and weak artificial bonds. Acta Geotech 16:1355–1376

Le H-K, Huang W-C, Chien C-C (2021) Exploring micromechanical behaviors of soft rock joints through physical and DEM modeling. Bull Eng Geol Env 80:2433–2446

Li X, Zhao J (2018) A unified CFD-DEM approach for modeling of debris flow impacts on flexible barriers. Int J Numer Anal Meth Geomech 42:1643–1670. https://doi.org/10.1002/nag.2806

Li X, Dong M, Li S, Shang Y (2019) Experimental and theoretical studies of the relationship between dry and humid normal restitution coefficients. J Aerosol Sci 129:16–27

Li Z, Li X, Yu J, Cao W, Liu Z, Wang M, Liu Z, Wang X (2020) Influence of existing natural fractures and beddings on the formation of fracture network during hydraulic fracturing based on the extended finite element method. Geomech. Geophys. Geo-energ. Geo-resour. 6(58). https://doi.org/10.1007/s40948-020-00180-y.

Li N, Zhou Y, Li H (2021) Experimental study for the effect of joint surface characteristics on stress wave propagation. Geomech. Geophys. Geo-energ. Geo-resour. 7(50). https://doi.org/10.1007/s40948-021-00235-8.

Ma T, Chen P, Zhao J (2016) Overview on vertical and directional drilling technologies for the exploration and exploitation of deep petroleum resources. Geomech Geophys Geo-Energ Geo-Resour 2(4):365–395

Marinack Jr MC, Musgrave RE, Higgs III CF (2013) Experimental investigations on the coefficient of restitution of single particles. Tribol Trans 56:572–580

Marzulli V, Torres Cisneros LA, di Lernia A, Cafaro F, Pöschel T (2020) Impact on granular bed: validation of discrete element modeling results by means of two-dimensional finite element analysis. Granular Matter 22(1):27

Melosh HJ, Collins GS (2005) Meteor crater formed by low-velocity impact, Nature 434(157). https://doi.org/10.1038/434157a.

Mindlin RD, Deresiewicz H (1953) Elastic spheres in contact under varying oblique force, Trans. ASME. J Appl Mech 20:327–344

Moriguchi S, Borja RI, Yashima A, Sawada K (2009) Estimating the impact force generated by granular flow on a rigid obstruction. Acta Geotech 4:57–71

Naghi Dehghan A, Goshtasbi K, Ahangari K, Jin Y (2014) Experimental investigation of hydraulic fracture propagation in fractured blocks. Bull Eng Geol Env 74:887–895

Oh J, Li Y, Mitra R, Canbulat I (2017) A numerical study on dilation of a saw-toothed rock joint under direct shear. Rock Mech Rock Eng 50(4):913–925

Patil D, Higgs III CF (2017) Experimental investigations on the coefficient of restitution for sphere-thin plate elastoplastic impact. J Tribol 140(1), 011406.

Peng J, Wong LNY, Teh CI (2017) Effects of grain size-to-particle size ratio on micro-cracking behavior using a bonded-particle grain-based model. Int J Rock Mech Min Sci 100:207–217

Peng J, Wong LNY, Teh CI (2018) A re-examination of slenderness ratio effect on rock strength: insights from DEM grain-based modelling. Eng Geol 246:245–254

Peng J, Wong LNY, Teh CI (2021) Influence of grain size on strength of polymineralic crystalline rock: new insights from DEM grain-based modeling. J Rock Mech Geotech Eng [Ahead of Print]. https://doi.org/10.1016/j.jrmge.2021.01.011.

Potyondy DO (2011) Parallel-bond refinements to match macro properties of hard rock. In Continuum and distinct element numerical modeling in geomechanics, Proceedings of Second International FLAC/DEM Symposium, Melbourne, Australia, 459–465.

Potyondy DO (2015) The bonded-particle model as a tool for rock mechanics research and application: current trends and future directions. Geosystem Engineering 18(1):1–28

Potyondy DO, Cundall PA (2004) A bonded-particle model for rock. Int J Rock Mech Min Sci 41(8):1329–1364

Sandeep CS, Luo L, Senetakis K (2020) Effect of grain size and surface roughness on the normal coefficient of restitution of single grains. Materials 814:1–13

Sandeep CS, Senetakis K, Cheung DKH, Choi CE, Wang Y, Coop MR, Ng CWW (2021) Experimental study on the coefficient of restitution of grain against block interfaces for natural and engineered materials. Can Geotech J 58(1):35–48

Sandeep CS, Senetakis K (2018) Effect of Young's modulus and surface roughness on the inter-particle friction of granular materials. Materials 11, 217.https://doi.org/10.3390/ma11020217.

Sandeep CS, Senetakis K (2019) An experimental investigation of the microslip displacement of geological materials. Comput Geotech 107:55–67

Shen WG, Zhao T, Crosta GB, Dai F (2017) Analysis of impact-induced rock fragmentation using a discrete element approach. Int J Rock Mech Min Sci 98:33–38

Shen WG, Zhao T, Zhao JD, Dai F, Zhou GD (2018) Quantifying the impact of dry debris flow against a rigid barrier by DEM analyses. Eng Geol 241:86–96

Shen WG, Zhao T, Dai F, Jiang M, Zhou GGD (2019) DEM analyses of rock block shape effects on the response of rockfall impact against a soil buffering layer. Eng Geol 249:60–70

Sivakugan N, Shukla SK, Das BM (2013) Rock mechanics: an introduction. CRC Press, Taylor & Francis Group, New York, USA.

Stronge WJ (2018) Impact mechanics. Cambridge University Press (second Edition). https://doi.org/10.1017/9781139050227

Suzuki A, Hakura S, Hamura T, Hattori M, Hayama R et al (2012) Laboratory experiments on crater scaling-law for sedimentary rocks in the strength regime. J Geophys Res Planets 117(E8). https://doi.org/10.1029/2012JE004064.

Tan DY, Feng WQ, Yin JH, Zhu ZH, Qin JQ (2021) Numerical study of retention efficiency of a flexible barrier in mitigating granular flow comparing with large-scale physical modeling test data. Acta Geotech 16:433–448

Tang ZC, Wong LNY (2016) Influences of normal loading rate and shear velocity on the shear behavior of artificial rock joints. Rock Mech Rock Eng 49(6):2165–2172

Tang H, Song R, Dong Y, Song X (2019) Measurement of restitution and friction coefficients for granular particles and discrete element simulation for the tests of glass beads. Materials 12(19):3170

Teufelsbauer H, Wang Y, Pudasaini SP, Borja RI, Wu W (2011) DEM simulation of impact force exerted by granular flow on rigid structures. Acta Geotech 6:119

Tomac I, Gutierrez M (2015) Micromechanics of proppants agglomeration during settling in hydraulic fractures. Journal of Petrol. Exploration and Production Technology 5:417–434

Uehara JS, Ambroso MA, Ojha RP, Durian DJ (2003) Low-speed impact craters in loose granular media. Phys Rev Lett 90, 149902.

Walsh AM, Holloway KE, Habdas P, de Bruyn JR (2003) Morphology and scaling of impact craters in granular media. Phys Rev Lett 91, 104301.

Wang Y, Tonon F (2011) Discrete element modeling of rock fragmentation upon impact in rock fall analysis. Rock Mech Rock Eng 44:23–35

Wang H, Sharma MM (2018) Modeling of hydraulic fracture closure on proppants with proppant settling. J Pet Sci Eng 171:636–645

Wang F, Li B, Chen Q, Zhang S (2019) Simulation of proppant distribution in hydraulically fractured shale network during shut-in periods. J Pet Sci Eng 178:467–474

Wang Y, Li X, Zhao B, Zhang Z (2020a) Numerical simulation of particle plugging in hydraulic fracture by element partition method. Int. J. Numer. Anal. Methods in Geom. 44(14):1857–1879.

Wang L, Zheng Z, Yu Y, Liu T, Zhang Z (2020b) Determination of the energetic coefficient of restitution of maize grain based on laboratory experiments and DEM simulations. Powder Technol 362:645–658

Wang S, Xiong X, Liu Y et al (2021) Stress–strain relationship of sandstone under confining pressure with repetitive impact. Geomech. Geophys. Geo-energ. Geo-resour. 7(39). https://doi.org/10.1007/s40948-021-00250-9.

Westwood RF, Toon SM, Styles P, Cassidy NJ (2017) Horizontal respect distance for hydraulic fracturing in the vicinity of existing faults in deep geological reservoirs: a review and modelling study. Geomech Geophys Geo-Energ Geo-Resour 3:379–391. https://doi.org/10.1007/s40948-017-0065-3

Xiao H, Liu S, Wang D (2016) Tribological properties of sliding shale rock–alumina contact in hydraulic fracturing. Tribol Lett 62(2):1–9

Xu Q, Yu Y, Liu R, Cheng W, Yang H (2021) Study on dynamic damage characteristics of coal under alternating hydraulic pressure. Bull Eng Geol Env 80:2385–2397

Yang W-M, Geng Y, Zhou Z-Q, Li L-P, Gao C-L et al (2020) DEM numerical simulation study on fracture propagation of synchronous fracturing in a double fracture rock mass. Geomech. Geophys. Geo-energ. Geo-resour. 6(39). https://doi.org/10.1007/s40948-020-00162-0.

Yang E, Bui HH, Nguyen GD, Choi CE, Ng CWW, De Sterck H, Bouazza A (2021) Numerical investigation of the mechanism of granular flow impact on rigid control structures. Acta Geotechnica [Published Online]. https://doi.org/10.1007/s11440-021-01162-4.

Yu K, Tafti D (2016) Impact model for micrometer-sized sand particles. Powder Technol 294:11–21

Zeng J, Li H, Zhang D (2016) Numerical simulation of proppant transport in hydraulic fracture with the upscaling CFD-DEM method. Journal of Natural Gas Science & Engineering 33:264–277. https://doi.org/10.1016/j.jngse.2016.05.030

Zhang ZX, Kou SQ, Jiang LG, Lindqvist PA (2000) Effects of loading rate on rock fracture: fracture characteristics and energy partitioning. Int J Rock Mech Min Sci 37:745–762

Zhang X-P, Wong LNY (2014) Displacement field analysis for cracking processes in bonded-particle model. Bull Eng Geol Env 73(1):13–21

Zhang F, Zhu H, Zhou H Guo J, Huang B (2017) Discrete-element-method/computational-fluid-dynamics coupling simulaiton of proppant embedment and fracture conductivity after hydraulic fracturing. SPE 22(2). https://doi.org/10.2118/185172-PA.

Zhang B, Ji B, Liu W (2018) The study on mechanics of hydraulic fracture propagation direction in shale and numerical simulation. Geomech Geophys Geo-Energ Geo-Resour 4:119–127. https://doi.org/10.1007/s40948-017-0077-z

Zhang H, Liu S, Xiao H (2019a) Sliding friction of shale rock on dry quartz sand particles. Friction 7(4):307–315

Zhang H, Liu S, Xiao H (2019b) Tribological properties of sliding quartz sand particle and shale rock contact under water and guar gum aqueous solution in hydraulic fracturing. Tribol Int 129:416–426

Zhang Y, Lu X, Zhang X, Li P (2019c) Numerical simulation of proppant transportation in hydraulic fracture based on DDPM-KTGF Model. ASME-JSME-KSME 2019 8th Joint Fluids Engineering Conference, San Francisco, USA. https://doi.org/10.1115/AJKFluids2019-5613.

Zheng W, Tannant DD (2019) Influence of proppant fragmentation on fracture conductivity - insights from three-dimensional discrete element modeling. J Pet Sci Eng 177:1010–1023

Zoback MD, Kohli AH (2019) Unconventional reservoir geomechanics: shale gas, tight oil, and induced seismicity. Cambridge University Press